Article

A Long Lifetime All-Organic Aqueous Flow Battery Utilizing TMAP-TEMPO Radical

Yahua Liu, Marc-Antoni Goulet, Liuchuan Tong, ..., Michael J. Aziz, Zhengjin Yang, Tongwen Xu

maziz@harvard.edu (M.J.A.)
yangzj09@ustc.edu.cn (Z.Y.)
twxu@ustc.edu.cn (T.X.)

HIGHLIGHTS

Highly soluble and long lifetime TMAP-TEMPO for pH 7 aqueous flow batteries

The posolyte features a concentration-independent capacity retention rate

Temporal capacity retention rate of >99.974% per h for over 1,000 cycles

Rational molecular design leads to improved stability

TMAP-TEMPO represents an extremely stable redox-active radical organic for an AORFB posolyte. An all-organic AORFB based on TMAP-TEMPO and BTMAP-Vi exhibits an OCV of 1.1 V and a long lifetime, featuring a concentration-independent temporal capacity retention rate of >99.974% per h, or a capacity retention rate of 99.993% per cycle over 1,000 consecutive cycles.

Chem

CellPress

Article

A Long Lifetime All-Organic Aqueous Flow Battery Utilizing TMAP-TEMPO Radical

Yahua Liu,[1] Marc-Antoni Goulet,[2] Liuchuan Tong,[3] Yazhi Liu,[1] Yunlong Ji,[3] Liang Wu,[1] Roy G. Gordon,[3] Michael J. Aziz,[2,*] Zhengjin Yang,[1,4,*] and Tongwen Xu[1,*]

SUMMARY

The massive-scale integration of renewable electricity into the power grid is impeded by its intrinsic intermittency. The aqueous organic redox flow battery (AORFB) rises as a potential storage solution; however, the choice of positive electrolytes is limited, and the aqueous-soluble organic positive redox-active species reported to date have short lifetimes. Here we report a stable organic molecule for the positive terminal, 4-[3-(trimethylammonio)propoxy]-2,2,6,6-tetramethylpiperidine-1-oxyl (TMAP-TEMPO) chloride, exhibiting high (4.62 M) aqueous solubility. When operated in a practical AORFB against a negative electrolyte comprising BTMAP-viologen at neutral pH, the flow cell displayed an open-circuit voltage of 1.1 volts and a Coulombic efficiency of >99.73%. The capacity retention rate is among the highest of all-organic AORFBs reported to date, at 99.993% per cycle over 1,000 consecutive cycles; the temporal capacity fade rate of 0.026% per h is independent of concentration.

INTRODUCTION

Because of the emissions from fossil fuel combustion, efforts have been devoted to creating a sustainable supply of energy for our modern lifestyle with a minimum carbon footprint.[1,2] Facilitated by technological breakthroughs, more electricity is generated from sunlight and wind with ever-increasing efficiencies and rapidly falling cost;[3–6] the massive-scale integration of energy from these renewable resources into the power grid becomes inevitable. However, if directly connected to the grid, the intrinsically intermittent nature of solar and wind energy will cause undesirable power fluctuations, which could potentially be solved by energy storage systems. To this end, numerous methods have been proposed to store electrical energy, among which flow batteries are garnering interest for longer discharge duration applications.[7–10] The energy content of flow batteries is stored externally in their electrolytes (the posolyte, i.e., the positive electrolyte, and the negolyte, i.e., the negative electrolyte). Therefore, their capital cost approaches the cost of these electrolytes at sufficiently long discharge duration. If sufficiently inexpensive electrolytes can be developed, flow batteries may reach costs below those of conventional battery technologies, such as lead-acid and lithium-ion. Within this framework, AORFBs, which store energy in water-soluble redox-active organic compounds composed of earth-abundant elements, may enable low electrolyte costs.[11–13]

Nevertheless, the lifetime of current AORFBs cannot currently meet the expected 20 years of service life for widespread market penetration.[9,14] Capacity fade of AORFBs is often the result of molecular decomposition of the organic reactants.[14]

The Bigger Picture

With the rapidly falling cost of photovoltaic and wind energy generation, grid-scale integration of renewable energy becomes inevitable. This, however, is impeded by the intrinsic intermittency of these renewable energy resources. Safe, cost-effective storage could solve this problem. Aqueous organic redox flow batteries (AORFBs), which store energy externally in low-cost electroactive water-soluble organic molecules, have emerged as promising for this application. Current AORFBs are limited by short lifetimes and the limited choices for redox-active material for the positive electrolyte. We report a long lifetime TMAP-TEMPO/BTMAP-Vi all-organic aqueous flow battery, the capacity retention rate of which is among the highest of all-organic AORFBs. We discuss the potential cause of the stabilization of the free radical posolyte molecule. The results we report here constitute an important step toward massive-scale intermittent renewable energy penetration into the future electric grid.

Chem

Progress has been made in recent years, especially for the negolyte. For the particular case of neutral-pH systems, the focus of the current work, the first neutral-pH AORFB employed a negolyte based on methyl viologen (MV).[15] MV was later shown to have a low capacity retention rate due to bimolecular annihilation.[16] By introducing positively charged functional groups to enhance Coulombic repulsion, the lifetime of an MV derivative, bis-(trimethylammonio) propyl viologen (BTMAP-Vi), was extended to a multi-year timescale (for more details on the stability of MV-derivatives see Supplemental Information).[16] An example of an MV derivative with intermediate stability is the 4,4'-(thiazolo[5,4-d]thiazole-2,5-diyl)bis(1-(3-(trimethylammonio) propyl)pyridin-1-ium).[11]

Despite the advancements achieved for synthesizing stable organic molecules for aqueous negolytes, little progress has been made in designing stable organic high-potential posolytes. In addition, the concentration-dependent cycling stability of electrolyte in AORFBs remains a long-standing obstacle,[11,15–18] and only a few studies conducted rigorous long-term cycling experiments (e.g., >500 cycles and >1 week).[19–21]

Here, we report an extremely stable variant of the radical posolyte molecule 4-[3-(trimethylammonio)propoxy]-2,2,6,6-tetramethylpiperidine-1-oxyl (TMAP-TEMPO) chloride (Figures 1A, S1, and S2) synthesized from low-cost ($5–6 kg^{-1})[9] 4-hydroxy-2,2,6,6-tetramethylpiperidin-1-oxyl (4-OH-TEMPO) by adding Coulombic repulsion to suppress bimolecular interactions and by eliminating functionalities that could potentially lead to molecular decomposition. TMAP-TEMPO chloride features a solubility of 4.62 M in water and a highly reversible single-electron oxidation potential at 0.81 (V) versus the standard hydrogen electrode (SHE), approaching the thermodynamic limit of water stability at neutral pH. When paired with BTMAP-Vi (Figures S3–S5), the TMAP-TEMPO/BTMAP-Vi battery has an open-circuit voltage (OCV) of 1.1 V and exhibits an extremely high capacity retention rate, at 99.993% per cycle over 1,000 consecutive cycles; the temporal capacity fade rate of 0.026% per h is independent of concentration.

RESULTS AND DISCUSSION

A cyclic voltammetry (CV) study of TMAP-TEMPO at a scan rate of 100 mV s^{-1} gave a reversible oxidation peak at 0.81 V versus SHE ($E_{1/2}$) in 1 M NaCl (Figure 1B). A peak separation of 58 mV was observed in good accordance with the theoretical value of a reversible single-electron redox reaction at pH 7 (59 mV), and the oxidation peak does not shift when the scan rate varies (Figure S5). Regardless of the electrode overpotential, the oxidation potential of TMAP-TEMPO, 0.81 V versus SHE, approaches the thermodynamic upper limit of water stability at pH 7 (oxygen evolution reaction, 0.816 V versus SHE). No oxygen generation was detected with a ppm-level sensitive oxygen detector when the experiment was conducted in a properly sealed environment.

Rotating disk electrode measurements of TMAP-TEMPO gave an oxidation rate constant (k_0) of 1.02×10^{-2} cm s^{-1} (Figure S6). The rate constants of both TMAP-TEMPO and BTMAP-Vi (Table 1) are much faster than those of most other inorganic, organic, or organometallic species (Table S1).

The promising electrochemical characteristics suggest that TMAP-TEMPO might make a suitable posolyte for an AORFB. We then assembled a neutral-pH AORFB, with a posolyte comprising TMAP-TEMPO chloride and a negolyte comprising

[1]CAS Key Laboratory of Soft Matter Chemistry, iChEM (Collaborative Innovation Center of Chemistry for Energy Materials), School of Chemistry and Material Science, University of Science and Technology of China, Hefei 230026, P.R. China
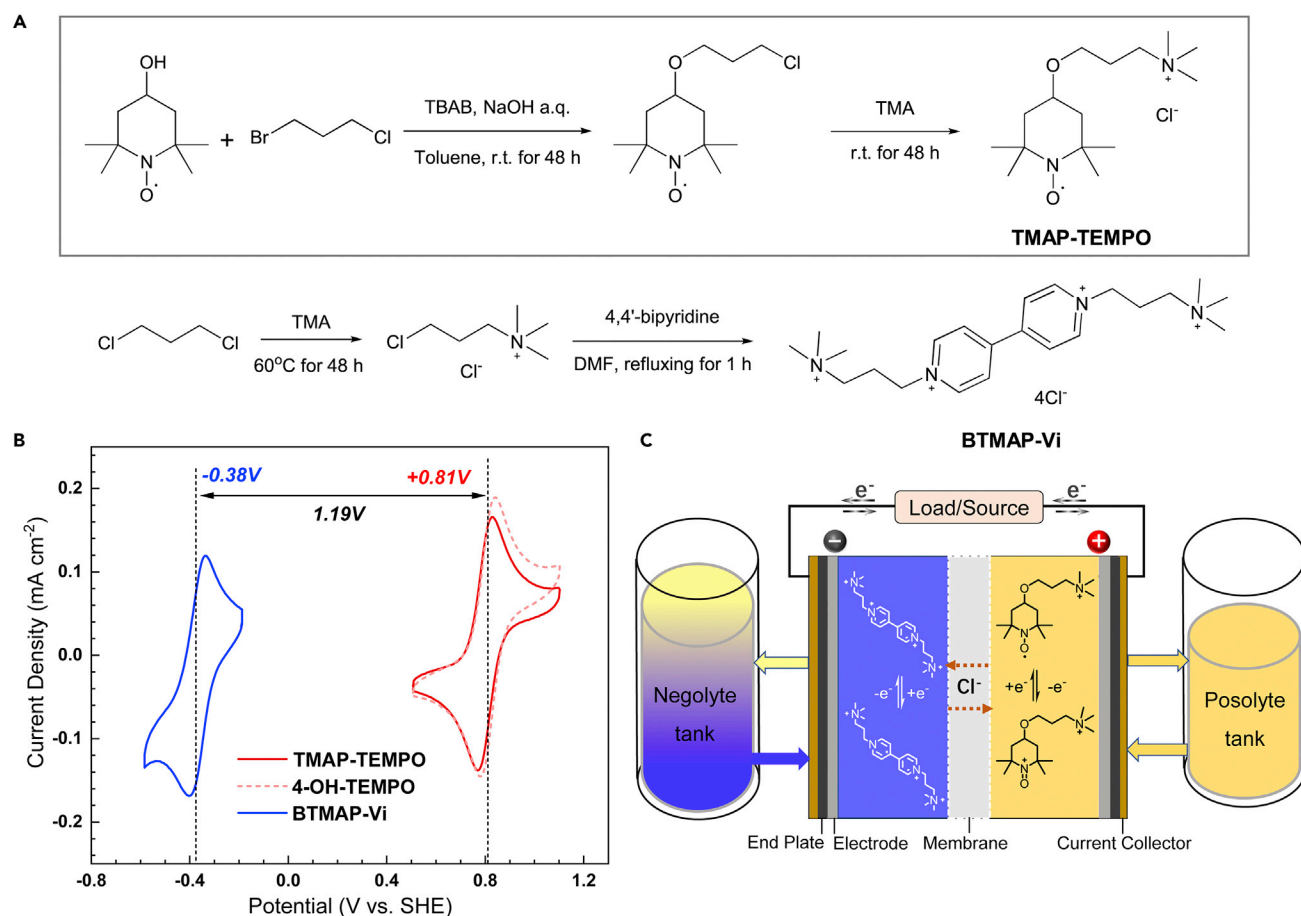
[2]Harvard John A. Paulson School of Engineering and Applied Sciences, 29 Oxford Street, Cambridge, MA 02138, USA

[3]Department of Chemistry and Chemical Biology, Harvard University, 12 Oxford Street, Cambridge, MA 02138, USA

[4]Lead Contact

*Correspondence: maziz@harvard.edu (M.J.A.), yangzj09@ustc.edu.cn (Z.Y.), twxu@ustc.edu.cn (T.X.)

Chem

Figure 1. Syntheses of TMAP-TEMPO and BTMAP-Vi and Their Potential Use as Electrolytes in AORFB

(A) Synthetic routes for TMAP-TEMPO and BTMAP-Vi.

(B) Cyclic voltammograms of TMAP-TEMPO (solid red trace), 4-OH-TEMPO (dashed light red trace), and BTMAP-Vi (solid blue trace). The electroactive compounds were tested at 1 mM in 1 M NaCl solution at a scan rate of 100 mV s^{-1}, on a glassy carbon working electrode.

(C) Schematic of a neutral flow battery assembled with TMAP-TEMPO in the posolyte and BTMAP-Vi in the negolyte, with chloride ions passing through a Selemion AMV anion-selective membrane.

BTMAP-Vi tetrachloride, separated by a Selemion® AMV anion-exchange membrane. In a typical charge process, electrons are withdrawn from the TMAP-TEMPO, flow along the external circuit, and combine with the negolyte, BTMAP-Vi, while Cl$^-$ ions serve as the internal charge carrier, migrating across the Selemion® AMV membrane (Figure 1C). TMAP-TEMPO (the posolyte side) is the capacity-limiting side, and as a reference, the 4-OH-TEMPO/BTMAP-Vi cell with the same electrolyte concentration was also assembled (Figure 2, for details see the Supplemental Information).

The total discharge capacity was 25.7 mAh, which corresponded to 95.9% of the theoretical capacity (26.8 mAh). The deviation between the theoretical and the measured value is attributed to the loss during material transfer and the electrode overpotential during the charge-discharge process. We then stepwise charged the cell at constant voltage (1.5 V) with a 10% increment in the state-of-charge (SOC) and measured the polarizations of the cell. The OCV at 50% SOC rests at around 1.10 V (Figure S7), which is slightly lower than expected from CV studies (1.19 V, Figure 1B).

Table 1. Electrochemical and Physicochemical Properties of TMAP-TEMPO, 4-OH-TEMPO, and BTMAP-Vi

Electrolyte	D (cm^2 s^{-1})	k_0 (cm s^{-1})	$E_{1/2}$ (V versus SHE)	Water Solubility (mol L^{-1})	Permeability (cm^2 s^{-1})[a]	Reference
TMAP-TEMPO	3.48×10^{-6}	1.02×10^{-2}	0.81	4.62	6.40×10^{-10} (AMV)	This work
4-OH-TEMPO	2.95×10^{-5}	2.60×10^{-4}	0.80	2.1	1.34×10^{-9} (AMV)	[6]
BTMAP-Vi	3.60×10^{-6}	2.20×10^{-2}	-0.36	2.0	6.70×10^{-10} (DSV)	[7]
			-0.38		5.20×10^{-11} (AMV)	This work

[a]Membrane names are included in the parentheses. Abbreviations are as follows: D, diffusion coefficient; k_0, electron-transfer rate constant; and $E_{1/2}$, redox potential.

At ~100% SOC, the peak galvanic power density of the cell reaches 99.03 mW cm^{-2} at a current density of 162.7 mA cm^{-2} (Figure 2D), which is nearly the same as that of the neutral FcNCl/MV cell (100 mW cm^{-2}) with comparable OCV (1.05 V).[17] The modest peak power density of the TMAP-TEMPO/BTMAP-Vi cell is due to high membrane resistance. The polarization area specific resistance of the entire cell at 50% SOC is 3.17 Ω cm^2, while high-frequency area specific resistance is 2.20 Ω cm^2 (Figure S8). The high contribution from the membrane is expected to decrease as highly anion-conductive membranes become available.

The TMAP-TEMPO/BTMAP-Vi cell was initially cycled at constant current densities of 10, 20, 40, and 60 mA cm^{-2} (Figure 2E). For each current density, 20 consecutive galvanostatic cycles were performed and we observed almost 100% Coulombic efficiency during 20 consecutive cycles. A capacity utilization of 97% and a round-trip energy efficiency of 93.41% were reached at the current density of 10 mA cm^{-2}.

Prolonged galvanostatic cycling was performed to probe the cycling lifetime of the cell and the stability of the posolyte. Both the TMAP-TEMPO/BTMAP-Vi cell and the reference cell were cycled at 40 mA cm^{-2} for 1,000 cycles (Figures 2B and 2F). The TMAP-TEMPO/BTMAP-Vi cell displayed a Coulombic efficiency of >99.73% and a significantly long cycling lifetime. The cell retained 94% of the initial capacity after 1,000 cycles, projecting a capacity retention rate of 99.993% per cycle or a temporal capacity retention rate of 99.974% per h (Figure 2F) or a loss rate of roughly 0.026% per h. In contrast, the reference cell lost 41% of its original capacity over 1,000 cycles (Figures 2B and S9–S12), projecting a temporal capacity loss rate of 0.22% per h, which is almost one order of magnitude higher than that of the TMAP-TEMPO/BTMAP-Vi cell.

The extended cycling lifetime of a flow battery could be the result of less membrane crossover of electroactive species or higher stability of the electroactive molecules. To understand the possible contribution from crossover, the permeabilities of 4-OH-TEMPO, TMAP-TEMPO, and BTMAP-Vi across a Selemion® AMV membrane were measured using a two-compartment diffusion cell (for details see the Supplemental Information; Figures S13–S15) and were determined to be 1.34×10^{-9} cm^2 s^{-1}, 6.40×10^{-10} cm^2 s^{-1}, and 5.20×10^{-11} cm^2 s^{-1}, respectively (Table 1). The lowered permeability for TMAP-TEMPO is consistent with its larger molecular radius and positive charge. The capacity-limiting TEMPO species show higher membrane permeabilities than that of the BTMAP-Vi. A CV study of the electrolyte after 1,000 consecutive cycles confirms the crossover of TMAP-TEMPO to the negolyte solution and BTMAP-Vi to the posolyte solution (Figure S16), even though the membrane crossover rate of either is very low.

Based on these measurements, we estimate that crossover contributed 39.6% of capacity lost in the TMAP-TEMPO cell, and only 9.4% of the capacity lost in the

Chem

CellPress
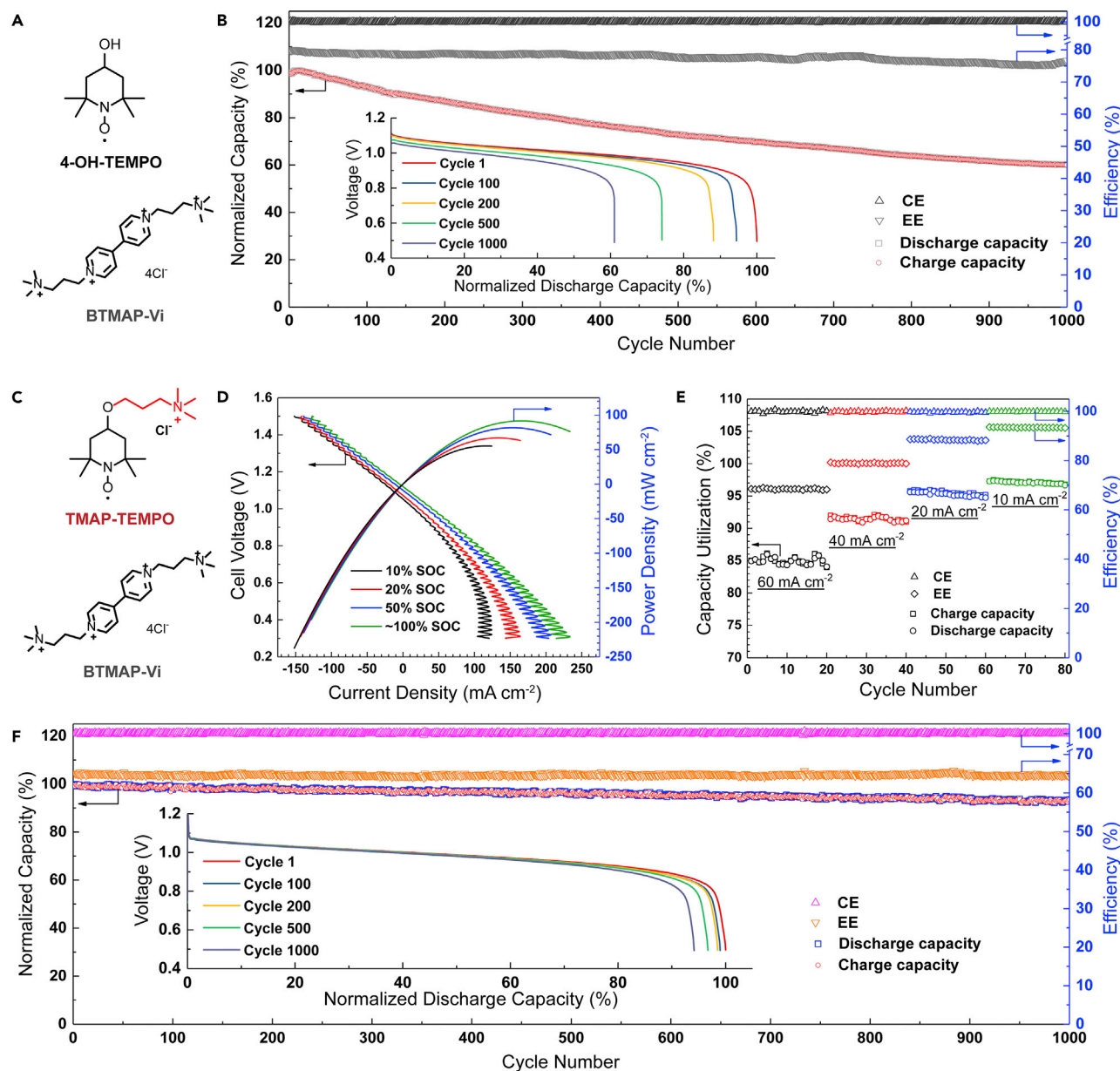
Figure 2. Performance of a Neutral-pH AORFB Assembled with Either 4-OH-TEMPO (0.1 M, A–B) or the Chloride Salt of TMAP-TEMPO (0.1 M, C–F) in Posolyte (10 mL) and BTMAP-Vi Tetrachloride (0.1 M) in Negolyte (15 mL, 1.5 Times e⁻ Excess)

(A) Structures of 4-OH-TEMPO and BTMAP-Vi.

(B) Galvanostatic cycling of the reference 4-OH-TEMPO/BTMAP-Vi cell at 40 mA cm⁻² for 1,000 consecutive cycles. Charge-discharge capacity, round-trip energy efficiency, and Coulombic efficiency (EE and CE, respectively) were plotted as functions of the cycle number. The entire 1,000 cycles occurred over a period of 191 h.

(C) Structures of TMAP-TEMPO and BTMAP-Vi.

(D) Polarization curves of the TMAP-TEMPO/BTMAP-Vi cell at varied SOC.

(E) Charge-discharge capacity, CE, and EE of the cell when galvanostatically cycled at current densities of 10, 20, 40, and 60 mA cm⁻², respectively.

(F) Galvanostatic cycling of the TMAP-TEMPO/BTMAP-Vi cell at 40 mA cm⁻² for 1,000 consecutive cycles. Charge-discharge capacity, EE and CE were plotted as functions of the cycle number. The entire 1,000 cycles occurred over a period of 220 h. (Insets in (B) and (F): the normalized discharge capacity of the cell at the 1st, the 100th, the 200th, the 500th, and the 1,000th cycle, respectively.)

reference cell because the capacity loss of 4-OH-TEMPO is so obvious. Hence, the slower crossover of TMAP-TEMPO accounts for merely a small fraction of the $\sim$10$\times$ slower capacity fade rate, namely 5.12% of the total savings of capacity loss (see the Supplemental Information, "Calculation of capacity loss due to electrolyte crossover"). This indicates that TMAP-TEMPO is structurally more stable than 4-OH-TEMPO.

The rest of the capacity loss is attributed to the chemical decomposition of TMAP-TEMPO. We hypothesize that the ring-opening side reactions on the nitroxide radicals of TMAP-TEMPO during galvanostatic charging or discharging is responsible for the loss of redox-active material.[22] The attack of water on the oxidized nitroxide radicals would open the ring but would not change the aliphatic hydrogens; this is consistent with the absence of new proton peaks in the ^{1}HNMR spectrum of the TMAP-TEMPO after cycling for 1,000 consecutive cycles (Figure S17).

To further investigate the source of capacity loss and eliminate the effect of crossover, we employed the unbalanced compositionally symmetric-cell cycling method by putting the same 50% SOC TMAP-TEMPO on both sides.[14] Over 25 days, 1,850 cycles, the cell lost roughly 14% of its initial capacity, equating to roughly 0.023% per h (Figures S18–S20), which is in reasonable agreement with the fade rate observed in the previously mentioned full-cell data.

Permeability analysis and the symmetric-cell results combine to establish the low fade rate of TMAP-TEMPO. Encouraged by the high capacity retention rate of TMAP-TEMPO/BTMAP-Vi at 0.1 M and the high water solubility of the electrolytes, we constructed a cell with a higher active concentration of 0.5 M for both sides. The concentrated TMAP-TEMPO/BTMAP-Vi cell showed a peak galvanic power density of 134 mW cm^{-2} (Figure 3A, EIS of the cell is presented in Figure S21) and exhibited Coulombic efficiencies of >99.9% at all current densities (Figure 3B). The cell was cycled continuously for 200 cycles at 100 mA cm^{-2} (Figures 3C and S22). After 200 cycles, the cell retained 95% of its original capacity, projecting a temporal capacity retention rate of 99.973% per h or a temporal capacity loss rate of 0.027% per h. The temporal capacity loss rate is nearly the same as that obtained from the TMAP-TEMPO/BTMAP-Vi cell at 0.1 M concentration, indicating a concentration-independent temporal capacity loss rate, which is in contrast to the results obtained for other radical posolytes.[11,15,18] Even at a higher electrolyte concentration of 1.5 M, the cell manifested a capacity retention rate of 99.985% per cycle, projecting a temporal capacity retention rate of 99.977% per h or a temporal capacity loss rate of 0.023% per h (Figure 4).

TMAP-TEMPO has a water solubility of 4.62 M (Supplemental Experimental Procedures), which corresponds to a theoretical posolyte capacity of 120 Ah L^{-1}. We expect the solubility of the oxidized form to be even higher because when oxidized, the molecule will bear one more positive charge and the molecular weight or motif remains unchanged. The solution has a viscosity of $\sim$580 mPa$\cdot$s at 4.5 M (a homogeneous solution as shown in Figure S23), which is higher than that of a polymeric electrolyte[12] and would compromise the overall efficiency of the system because of pumping loss. The viscosity at 0.5 M is only 3.58 mPa$\cdot$s (Figure S21B).

When taken together, the long-term galvanostatic cycling results, symmetric-cell cycling results, and permeability measurements suggest that TMAP-TEMPO is exceptionally stable. This stability might be due to any of several possible causes,
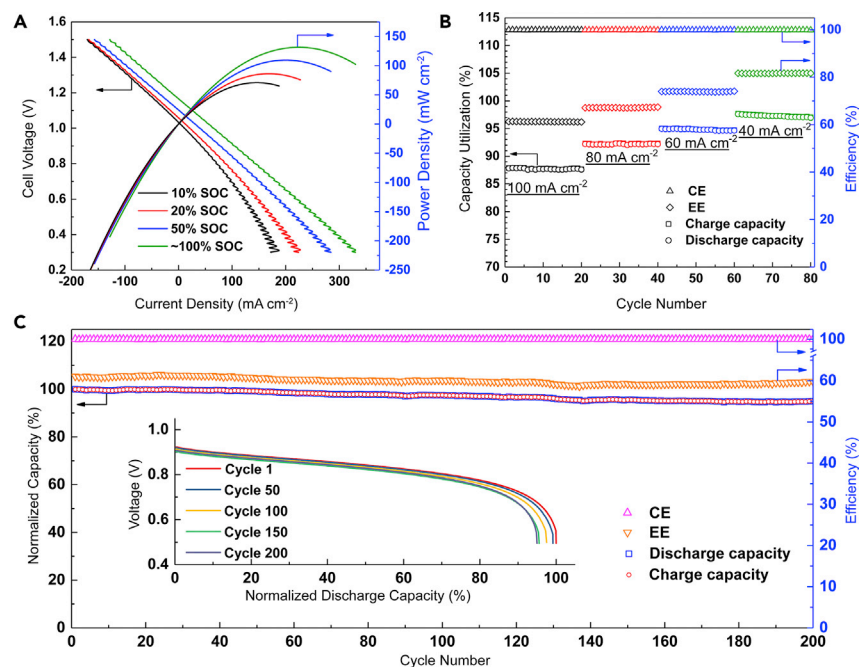
Figure 3. Performance of Concentrated TMAP-TEMPO/BTMAP-Vi Cell Assembled with TMAP-TEMPO Chloride (0.5 M) in Posolyte (10 mL) and BTMAP-Vi Tetrachloride (0.5 M) in Negolyte (15 mL)
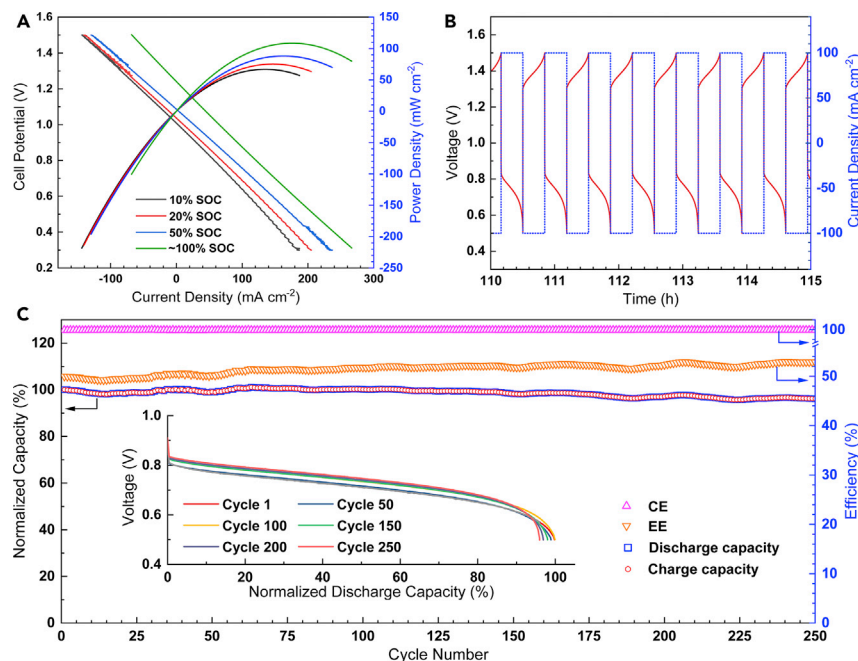
(A) Polarizations of the cell at varied SOC.

(B) Charge-discharge capacity, CE and EE of the cell when galvanostatically cycled at current densities of 100, 80, 60, and 40 mA cm^{-2}, respectively.

(C) Galvanostatic cycling of the cell at 100 mA cm^{-2} for 200 consecutive cycles. Charge-discharge capacity, EE, and CE are plotted as functions of the cycle number. Inset: the normalized discharge capacity of the cell at the 1st, the 50th, the 100th, the 150th, and the 200th cycle, respectively. Total discharge capacity of the cell on the first discharge is 446.1 C, which is 93% of the theoretical value. The entire 200 cycles occurred over a period of 80.6 h.

namely steric hindrance, Coulombic repulsion, and electronic isolation of the charged functional groups. The plausible mechanisms are provided as follows. The four peripheral methyl groups provide steric hindrance, which could suppress possible interactions between the free radicals. Additionally, the Coulombic repulsion between the positively charged TMAP-TEMPO molecules might also reduce bimolecular or multi-molecular interaction. Prior work with 4-OH-TEMPO[15] and TEMPO-4-ammonium (TEMPTMA,[18] also known as N^{Me}-TEMPO[11]) and TEMPO-4-sulfate[23] exhibited lifetimes that decreased with increasing concentration, whereas in our system, concentration-independent lifetime with TMAP-TEMPO was observed. This suggests that the TMAP-TEMPO has suppressed bimolecular or multi-molecular annihilation and may follow a decomposition mechanism that is only first order on TMAP-TEMPO concentration. Finally, attaching a charge directly to the 6-membered ring might compromise the stability of the molecules because the electronic effect, especially a strong one, could make the joint weak and susceptible to ring-opening side reactions. This is more consistent with the longer lifetime of TMAP-TEMPO than with that of TEMPTMA,[18] to which the positively charged ammonium is directly attached, or with that of TEMPO-4-sulfate,[23] to which the negatively charge sulfate is directly attached. The use of aliphatic spacers may mitigate ring-opening side reactions caused by the electronic effect of the charged functionalities.

Figure 4. Performance of High Concentration TMAP-TEMPO/BTMAP-Vi Cell Assembled with TMAP-TEMPO Chloride (1.5 M) in Posolyte and BTMAP-Vi Tetrachloride (1.5 M) in Negolyte.

(A) Polarizations of the cell at varied SOC.

(B) Representative cell voltage and charge-discharge current density versus time during cycling at 100 mA cm^{-2}.

(C) Galvanostatic cycling of the cell at 100 mA cm^{-2} for 250 consecutive cycles. Charge-discharge capacity, EE, and CE are plotted as functions of the cycle number. Inset: the normalized discharge capacity of the cell at the 1st, the 50th, the 100th, the 150th, the 200th, and the 250th cycle, respectively. Total discharge capacity of the cell on the first discharge is 625.0 C. The entire 250 cycles occurred over a period of 171.7 h.

TMAP-TEMPO/BTMAP-Vi is among the most stable all-organic AORFB chemistry to date, but we note that there are longer-lifetime AORFBs at high pH in which the posolyte utilizes the inorganic redox couple ferricyanide-ferrocyanide,[21] and at neutral pH in which the posolyte comprises the organometallic redox couple FcNCl,[17] and an even longer-lifetime functionalization, BTMAP-Fc.[16] A critical question is whether there is a fundamental reason that voltage trades off against lifetime, or whether it is possible to enhance both. This question is apparent if one examines OCVs and lifetimes among ferrocene-based batteries and does the same for TEMPO-based ones. The FcNCl/MV cell (OCV 1.06 V) has a temporal capacity fade rate of 0.078% per h, while the low-OCV version, BTMAP-Fc/BTMAP-Vi (OCV 0.75 V) shows greatly enhanced lifetime with a temporal capacity fade rate of 0.0042% per h. Similarly, TMAP-TEMPO/BTMAP-Vi (OCV 1.19 V) has a temporal capacity fade rate that is half that of TEMPTMA/MV (OCV 1.42 V) and is less than one-fourth that of N^{Me}-TEMPO/[(NPr)$_2$TTz]Cl$_4$ (OCV 1.44 V) (Table S2). Better understanding of capacity fade mechanisms will likely be necessary before this question can be answered.

In summary, we have synthesized an extremely stable redox-active radical organic for an AORFB posolyte, TMAP-TEMPO, which has >4.5 M solubility in water. An all-organic AORFB based on TMAP-TEMPO and BTMAP-Vi exhibits an OCV of 1.1 V and exhibits exceptionally long lifetime. It features a concentration-independent temporal capacity retention rate of >99.974% per h, or a capacity retention rate of 99.993% per cycle over 1,000 consecutive cycles. Symmetric-cell testing

Chem

established the low fade rate of TMAP-TEMPO. We anticipate that by improving the ion selective membrane, the entire cell resistance might be greatly reduced, thereby increasing the power density, and the membrane crossover rate of electroactive species might be reduced, thereby further increasing the capacity retention rate. Our results constitute an important step toward massive-scale intermittent renewable energy penetration into the future electric grid.

SUPPLEMENTAL INFORMATION

Supplemental Information can be found online at https://doi.org/10.1016/j.chempr.2019.04.021.

AUTHOR CONTRIBUTIONS

Z.Y., M.J A., and T.X. designed the project. Y.L., Y.J., L.T., and Z.Y. synthesized the compounds. Y.L. and M.-A.G. collected the experimental data. Z.Y., Y.L., M.-A.G., L.T., R.G.G., M.J.A., L.W., Y.L., and T.X. analyzed the experimental results and helped with discussions. Z.Y., Y.L., M.-A.G., T.X., and M.J.A. wrote the paper, and all authors contributed to revising the paper.

DECLARATION OF INTERESTS

The authors declare no competing interests.

REFERENCES AND NOTES

1. Armand, M., and Tarascon, J.M. (2008). Building better batteries. Nature 451, 652–657.

2. Obama, B. (2017). The irreversible momentum of clean energy. Science 355, 126–129.

3. Arora, N., Dar, M.I., Hinderhofer, A., Pellet, N., Schreiber, F., Zakeeruddin, S.M., and Grätzel, M. (2017). Perovskite solar cells with CuSCN hole extraction layers yield stabilized efficiencies greater than 20%. Science 358, 768–771.

4. Hou, Y., Du, X., Scheiner, S., McMeekin, D.P., Wang, Z., Li, N., Killian, M.S., Chen, H., Richter, M., Levchuk, I., et al. (2017). A generic interface to reduce the efficiency-stability-cost gap of perovskite solar cells. Science 358, 1192–1197.

5. Yang, W.S., Park, B.W., Jung, E.H., Jeon, N.J., Kim, Y.C., Lee, D.U., Shin, S.S., Seo, J., Kim, E.K., Noh, J.H., et al. (2017). Iodide management in formamidinium-lead-halide–based perovskite layers for efficient solar cells. Science 356, 1376–1379.

6. Bush, K.A., Palmstrom, A.F., Yu, Z.J., Boccard, M., Cheacharoen, R., Mailoa, J.P., McMeekin, D.P., Hoye, R.L.Z., Bailie, C.D., Leijtens, T., et al. (2017). .23.6%-efficient monolithic perovskite/silicon tandem solar cells with improved stability. Nat. Energy 2, 17009.

7. Wang, W., Luo, Q.T., Li, B., Wei, X.L., Li, L.Y., and Yang, Z.G. (2013). Recent progress in redox flow battery research and development. Adv. Funct. Mater 23, 970–986.

8. Soloveichik, G.L. (2015). Flow batteries: current status and trends. Chem. Rev. 115, 11533–11558.

9. Winsberg, J., Hagemann, T., Janoschka, T., Hager, M.D., and Schubert, U.S. (2017). Redox-flow batteries: from metals to organic redox-active materials. Angew. Chem. Int. Ed. 56, 686–711.

10. Noack, J., Roznyatovskaya, N., Herr, T., and Fischer, P. (2015). The chemistry of redox-flow batteries. Angew. Chem. Int. Ed. 54, 9776–9809.

11. Luo, J., Hu, B., Debruler, C., and Liu, T.L. (2018). A pi-conjugation extended viologen as a two-electron storage anolyte for total organic aqueous redox flow batteries. Angew. Chem. Int. Ed. 57, 231–235.

12. Janoschka, T., Martin, N., Martin, U., Friebe, C., Morgenstern, S., Hiller, H., Hager, M.D., and Schubert, U.S. (2015). An aqueous, polymer-based redox-flow battery using non-corrosive, safe, and low-cost materials. Nature 527, 78–81.

13. Lin, K., Chen, Q., Gerhardt, M.R., Tong, L., Kim, S.B., Eisenach, L., Valle, A.W., Hardee, D., Gordon, R.G., Aziz, M.J., et al. (2015).

Alkaline quinone flow battery. Science *349*, 1529–1532.

14. Goulet, M.A., and Aziz, M.J. (2018). Flow battery molecular reactant stability determined by symmetric cell cycling methods. J. Electrochem. Soc. *165*, A1466–A1477.

15. Liu, T.B., Wei, X.L., Nie, Z.M., Sprenkle, V., and Wang, W. (2016). A total organic aqueous redox flow battery employing a low cost and sustainable methyl viologen anolyte and 4-HO-TEMPO catholyte. Adv. Energy Mater *6*.

16. Beh, E.S., De Porcellinis, D., Gracia, R.L., Xia, K.T., Gordon, R.G., and Aziz, M.J. (2017). A neutral pH aqueous organic–organometallic redox flow battery with extremely high capacity retention. ACS Energy Lett. *2*, 639–644.

17. Hu, B., DeBruler, C., Rhodes, Z., and Liu, T.L. (2017). Long-cycling aqueous organic redox

flow battery (AORFB) toward sustainable and safe energy storage. J. Am. Chem. Soc. *139*, 1207–1214.

18. Janoschka, T., Martin, N., Hager, M.D., and Schubert, U.S. (2016). An aqueous redox-flow battery with high capacity and power: the TEMPTMA/MV system. Angew. Chem. Int. Ed. *55*, 14427–14430.

19. Murali, A., Nirmalchandar, A., Krishnamoorthy, S., Hoober-Burkhardt, L., Yang, B., Soloveichik, G., Prakash, G.K.S., and Narayanan, S.R. (2018). Understanding and mitigating capacity fade in aqueous organic redox flow batteries. J. Electrochem. Soc. *165*, A1193–A1203.

20. Ji, Y., Goulet, M.A., Pollack, D.A., Kwabi, D.G., Jin, S., Porcellinis, D., Kerr, E.F., Gordon, R.G., and Aziz, M.J. (2019). A phosphonate-functionalized quinone redox flow battery at

near-neutral pH with record capacity retention rate. Adv. Energy Mater. *9*.

22. Ma, Y., Loyns, C., Price, P., and Chechik, V. (2011). Thermal decay of TEMPO in acidic media via an N-oxoammonium salt intermediate. Org. Biomol. Chem. *9*, 5573–5578.

23. Winsberg, J., Stolze, C., Schwenke, A., Muench, S., Hager, M.D., and Schubert, U.S. (2017). Aqueous 2,2,6,6-Tetramethylpiperidine-N-oxyl catholytes for a high-capacity and high current density oxygen-insensitive hybrid-flow battery. ACS Energy Lett. *2*, 411–416.

21. Kwabi, D.G., Lin, K., Ji, Y., Kerr, E.F., Goulet, M.-A., DePorcellinis, D., Tabor, D.P., Pollack, D.A., Aspuru-Guzik, A., Gordon, R.G., et al. (2018). Alkaline quinone flow battery with long lifetime at pH 12. Joule *2*, 1894–1906.

Supplemental Figures and Tables
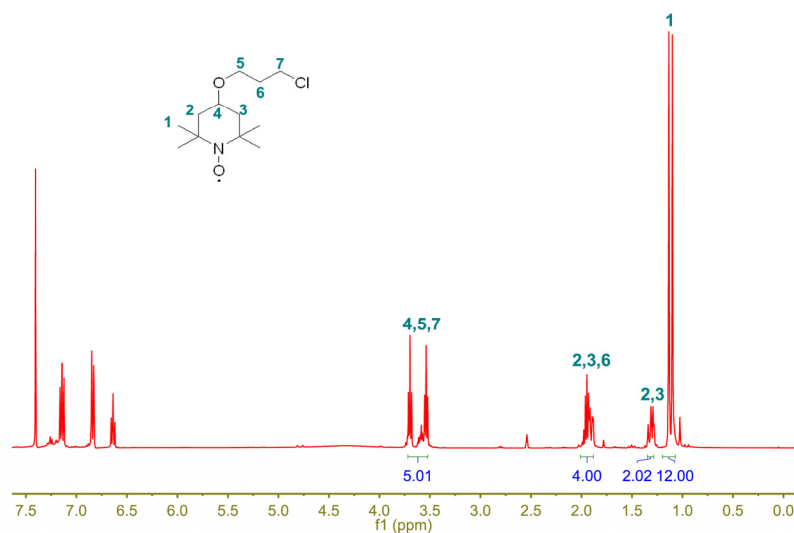
Figure S1. ^{1}H NMR spectrum of Pr-TEMPO, recorded in d6-DMSO. The asterisk indicates the signal from the solvent.
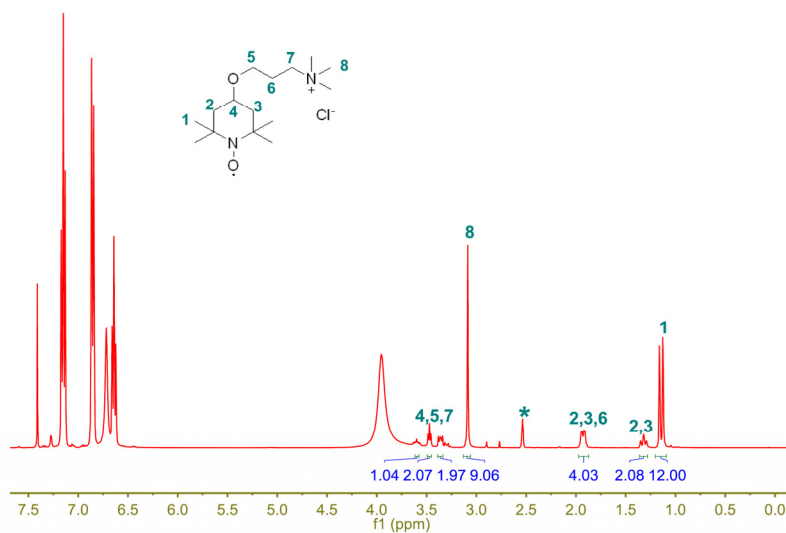

Figure S2. ^{1}H NMR spectrum of TMAP-TEMPO, recorded in d6-DMSO. TMAP-TEMPO was reduced by phenyl hydrazine prior to characterization and the peaks in the region from 6.5 ppm to 7.5 ppm belongs to phenyl hydrazine. The asterisk indicates the signal from the solvent.
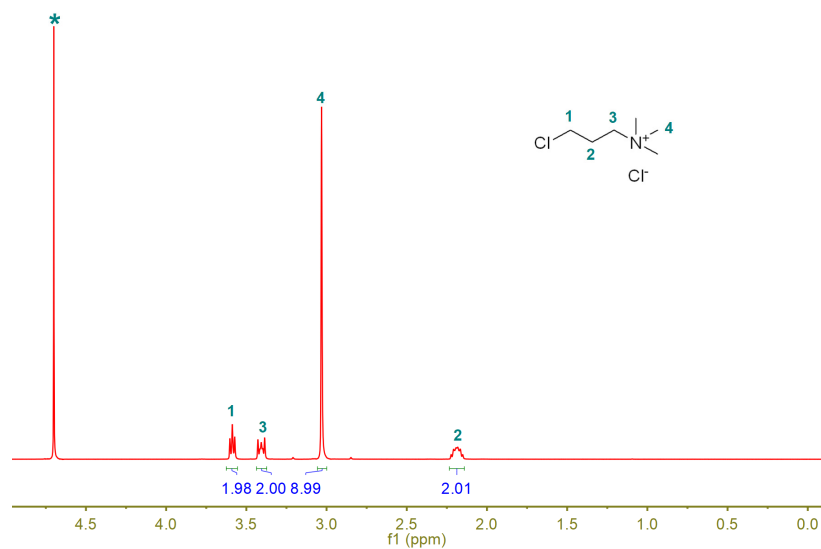
Figure S3. ^{1}H NMR spectrum of (3-chloro-propyl)-trimethyl-ammonium chloride, recorded in D$_2$O. The asterisk indicates the signal from the solvent.
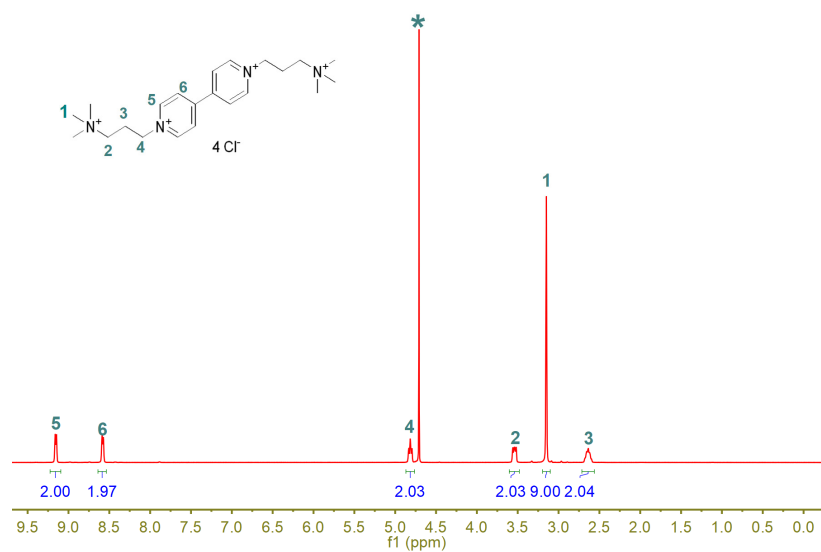
Figure S4. ^{1}H NMR spectrum of BTMAP-Vi, recorded in D$_2$O. The asterisk indicates the signal from the solvent.
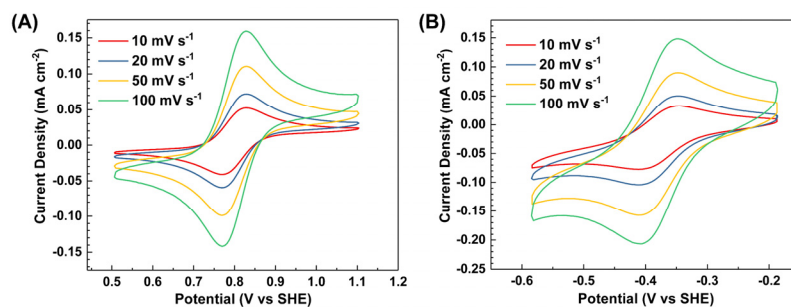
Figure S5. Cyclic voltammograms of (A) 1 mM TMAP-TEMPO in 1 M NaCl solution and (B) 1 mM BTMAP-Vi in 1 M NaCl solution at various potential scanning rates. Potential was referenced to standard hydrogen electrode (SHE).
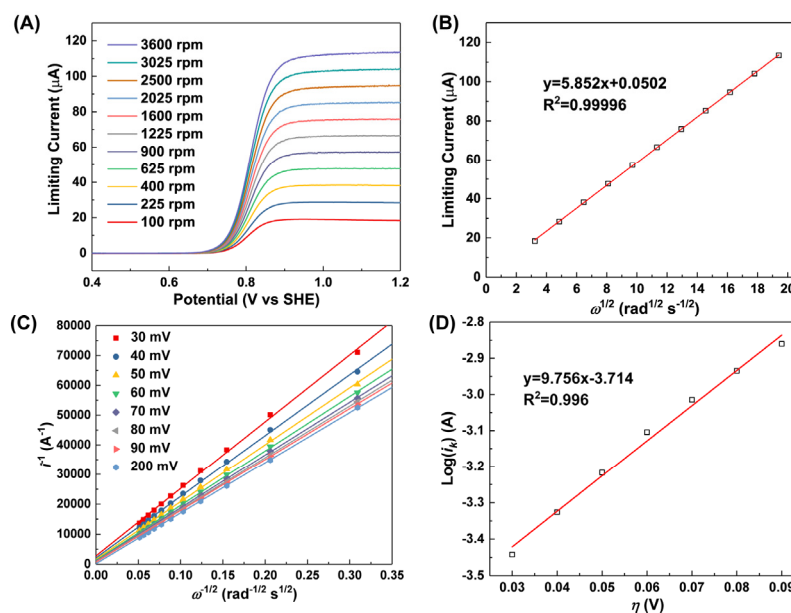
Figure S6. Rotating-disk-electrode experiment on TMAP-TEMPO (1 mM in 1 M NaCl). (A) Current versus potential at rotation rates from 100 to 3600 rpm with potential sweeping rate of 5 mV s^{-1}. (B) Levich plot of limiting current versus square root of rotation rate ($\omega^{1/2}$). (C) Koutecky–Levich plot at different overpotentials; reciprocal of kinetically limited current is indicated on vertical axis. (D) Tafel plot, the logarithm of kinetically limited current versus overpotential (potential deviation from the formal reduction potential.
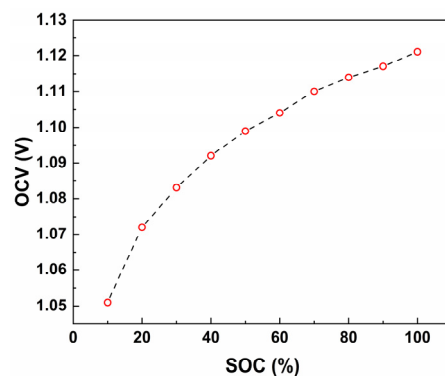
Figure S7. Open-circuit voltage (OCV) of a TMAP-TEMPO/BTMAP-Vi cell at pH 7 at various states of charge (SOC).
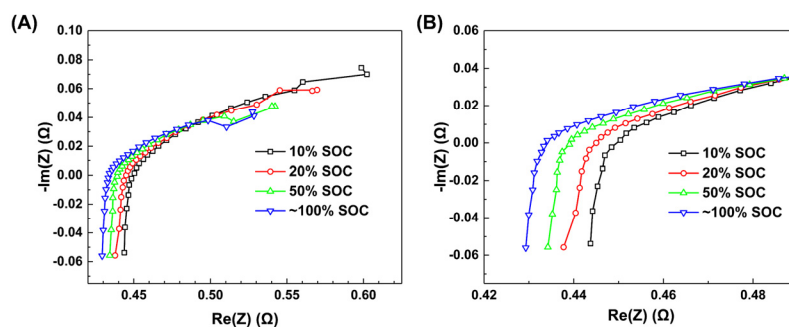
Figure S8. Electrochemical impedance spectroscopy (EIS) of AMV inside a TMAP-TEMPO/BTMAP-Vi cell (0.1 M) (A) at frequencies ranging from 1 Hz to10 kHz and (B) a zoomin of EIS near y=0. The AC-ASR (high frequency resistance) was 2.20 Ω cm^2, determined by the intersection of the curves at y=0.
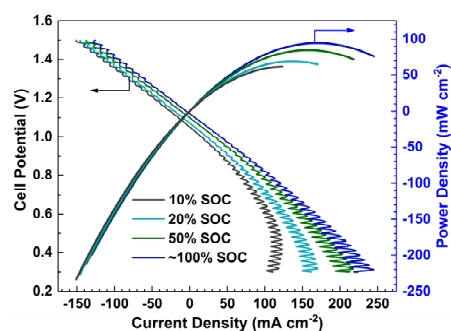

Figure S9. Polarization curves of the 4-OH-TEMPO/BTMAP-Vi cell (0.1 M) at varied states of charge (SOC).
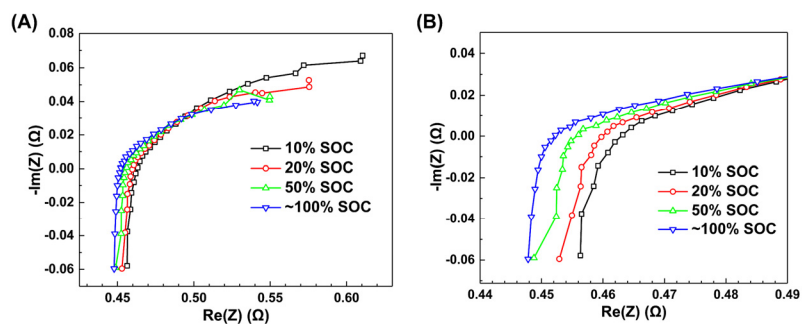
Figure S10. Electrochemical impedance spectroscopy (EIS) of AMV inside a 4-OH-TEMPO/BTMAP-Vi cell (0.1 M) (A) at frequencies ranging from 1 Hz to10k Hz and (B) a zoomin near y=0. The AC-ASR (high frequency resistance) was 2.28 Ω cm^2.
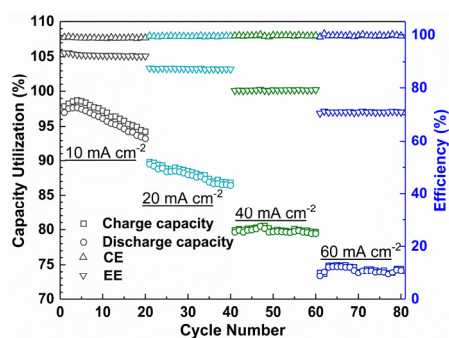
Figure S11. Charge/discharge capacity, coulombic efficiency (CE) and round-trip energy efficiency (EE) of 4-OH-TEMPO/BTMAP-Vi cell when galvanostatically cycled at current densities of 10, 20, 40 and 60 mA cm^{-2}, respectively; for each current density, 20 consecutive cycles were performed.
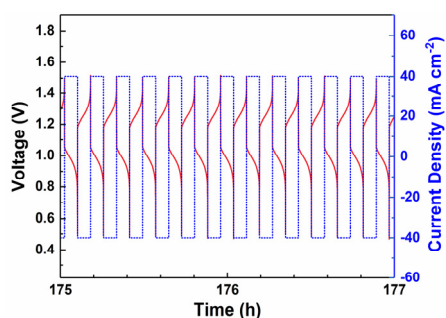
Figure S12. Representative cell voltage and charge/discharge current density vs. time curves during galvanostatic cycling at 40 mA cm^{-2} for 4-OH-TEMPO/BTMAP-Vi cell.
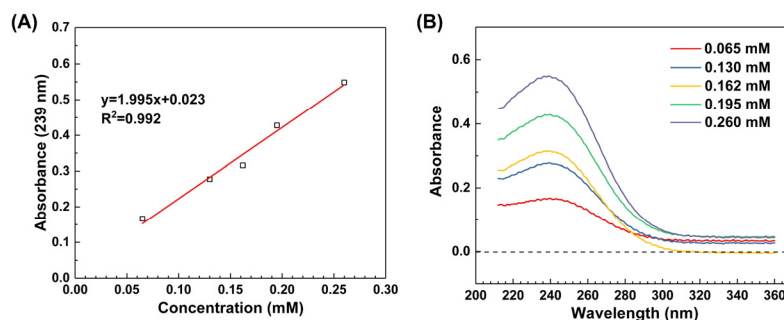
Figure S13. UV-Vis calibration lines for determination of the concentration of TMAP-TEMPO solution. (A) The UV-Vis absorbance of TMAP-TEMPO at 239 nm versus the concentration of its aqueous solution; (B) UV-Vis spectra of TMAP-TEMPO of different concentrations in 1 M NaCl aqueous solution.
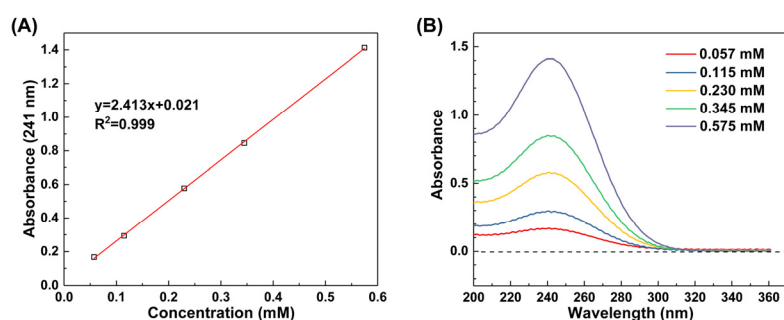

Figure S14. UV-Vis calibration lines for determination of the concentration of 4-OH-TEMPO solution. (A) The absorbance at 241 nm of 4-OH-TEMPO versus the concentration of 4-OH-TEMPO aqueous solution, (B) UV-Vis spectra of 4-OH-TEMPO of different concentrations in 1 M NaCl aqueous solution
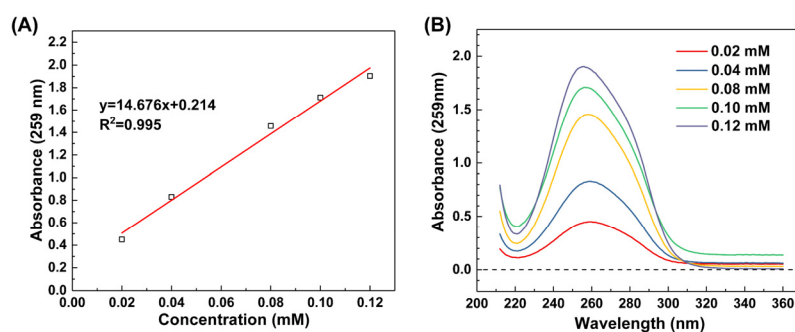
Figure S15. UV-Vis calibration lines for determination of the concentration of BTMAP-Vi solutions. (A) The absorbance at 259 nm of BTMAP-Vi versus the concentration of its aqueous solution, (B) UV-Vis spectra of BTMAP-Vi of different concentrations in 1 M NaCl aqueous solution.
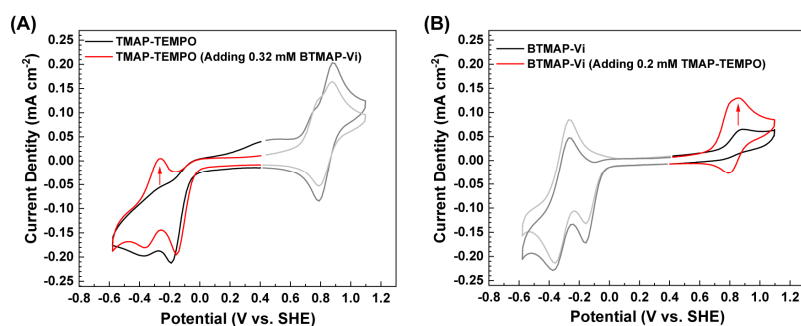
Figure S16. Cyclic voltammetry analyses of posolyte (TMAP-TEMPO) and the negolyte (BTMAP-Vi) after 1000-consecutive cycles at 40 mA cm^{-2}; the electrolyte concentration is 0.1 M for cell cycling. (A) Cyclic voltammograms of cycled TMAP-TEMPO (black trace and dark grey trace). The grey traces in the high-potential region indicate the redox reaction of TMAP-TEMPO. The black trace in the low-potential region suggests the migration of BTMAP-Vi from the negolyte to the posolyte. To confirm the migration of BTMAP-Vi, 0.32 mM of additional BTMAP-Vi was added to the cycled posolyte, resulting in the red trace and the light grey trace. (B) Cyclic voltammograms of cycled BTMAP-Vi (black trace and dark grey trace). The grey traces in the low-potential region indicate the redox reaction of BTMAP-Vi. The black trace in the high-potential region suggests the migration of TMAP-TEMPO from the posolyte to the negolyte. To confirm the migration of TMAP-TEMPO, 0.2 mM of additional TMAP-TEMPO was further added to the cycled negolyte, resulting in the red trace and the light grey trace.
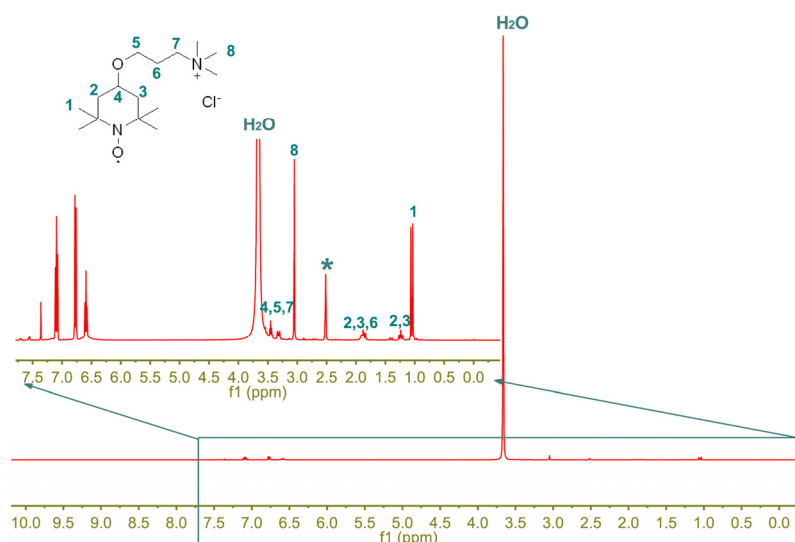

Figure S17. ^{1}H NMR spectrum of the posolyte, TMAP-TEMPO, after 1000-consecutive galvanostatic cycles; aliquots were directly taken from the reservoir, diluted with and recorded in d6-DMSO. TMAP-TEMPO was reduced by phenyl hydrazine prior to characterization and the peaks in the region from 6.5 ppm to 7.5 ppm belong to phenyl hydrazine. The asterisk indicates the signal from the solvent. And there is a strong peak corresponding to H$_2$O from the posolyte solution.
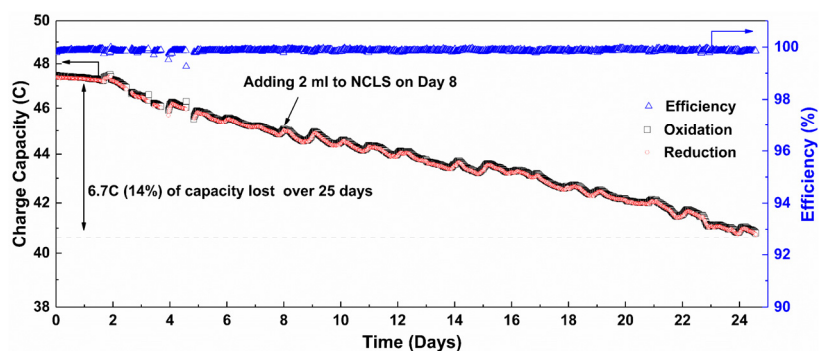
Figure S18. Semi-log plot of unbalanced compositionally-symmetric cell with 0.1M TMAP-TEMPO in 1M NaCl exhibiting an average capacity fade rate of 0.023%per hour. The entire1850 cycles occurred over a period of 25 days. Coulombic efficiency is displayed on the right axis.
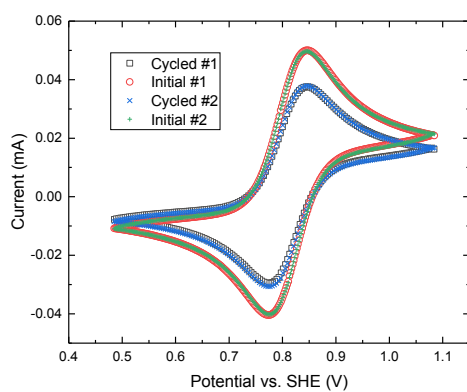
Figure S19. IR-corrected cyclic voltammograms of initial and cycled electrolytes, 0.1 M TMAP-TEMPO in 1 M NaCl. For each case, two separate aliquots were tested with 1 M NaCl background voltammograms taken between each measurement. Reduction of CV peak height for cycled electrolyte indicates loss of redox activity. For both oxidation and reduction, cycled electrolyte peak heights are 24% lower than those of initial electrolyte.
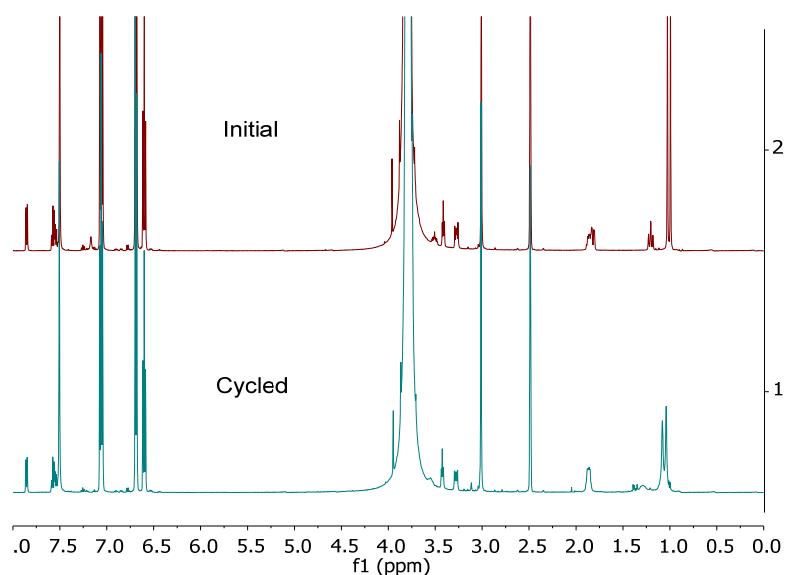
Figure S20. Stacked ^{1}H NMR spectra of initial TMAP-TEMPO electrolyte and CLS of symmetric cell after 25 days of cycling. 100 μl aliquots were directly taken from initial and cycled electrolytes and diluted in 700 μL d6-DMSO with phenyl hydrazine. Integration of TMAP-TEMPO peaks were compared by using non-deuterated DMSO peak as internal standard. All peaks of cycled electrolyte show loss of integration area of roughly 10-20% for TMAP-TEMPO peaks with respect to initial electrolyte. No indication of new decomposition peaks in cycled electrolyte.

As shown in Supplemental Figure S18, the capacity starts around 47.5 C which is 98.5% of the theoretical capacity of the CLS. Over 25 days and 1850 cycles the cell lost roughly 14% of this initial capacity, equating to roughly 0.023% per hour, which is in reasonable agreement with the fade rate observed in the previously mentioned full cell data. A relatively constant difference between oxidation and reduction capacities is observed during the entire test which averages to 0.056 C per cycle. As described in a previous study, this difference is attributed to potentiostat current bias and is uncorrelated with the capacity fade trend (i.e.: 0.056 C of capacity loss per cycle would lead to ten times higher fade rate than we observe) [1]. As observed for ferricyanide, an inorganic posolyte molecule, in the same previous study, the sudden change in fade rate around day 4 in Supplemental Figure S18 suggests that the NCLS may have become limiting. To check for this possibility, an additional 2 mL of initial 50% SOC electrolyte was added to the NCLS around day 8 as indicated in the graph. This 20% addition to the NCLS did not produce any measurable increase in capacity, however, which indicates that the capacity loss is due to the CLS rather than the NCLS and therefore may not be recoverable. To confirm this, the CLS electrolyte was analyzed after the 25 days of cycling by cyclic voltammetry and NMR. Although comparable, the loss (23%) of redox activity of the cycled electrolyte indicated by CV (Figure S19) is somewhat higher than the capacity lost during cycling (14%), which could be due to dilution of the CLS by water crossover. It should be noted that the pH of the CLS electrolyte had changed from the initial pH 7, to pH 3 by the end of cycling, which could have contributed to such water crossover. As with the full cell data, the NMR spectrum of the cycled electrolyte shows no clear sign of decomposition into other

molecules as indicated by the lack of new peaks in the aliphatic region (Figure S20). However, the integration of the cycled TMAP-TEMPO peaks has lost about 10-20% of its area with respect to the initial electrolyte, further indicating a loss in concentration. With a clear loss of capacity, redox activity and concentration but with no sign of a decomposition product, we suggest that the molecule is degraded due to water attack and the generated active hydrogens (OH, NH) are not easy to observe via NMR. It is unusual for potentiostatic symmetric cell cycling to produce such large fluctuations in measured capacity, and temperature fluctuations were investigated as a possible cause. A thermocouple inserted into the current collector of the cell revealed only 1℃ fluctuations over a week of cycling with no correlation to the capacity data.
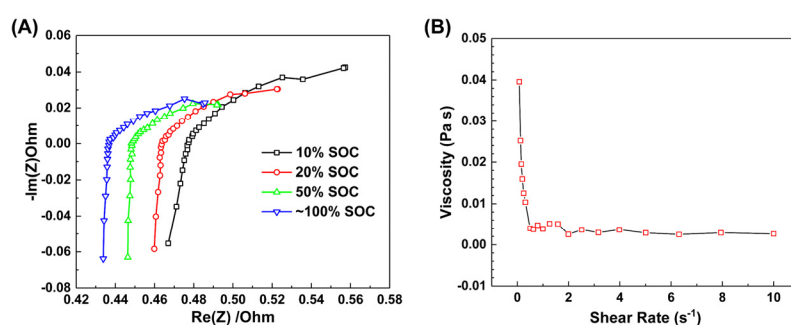
Figure S21. Electrochemical impedance spectroscopy (EIS) of a TMAP-TEMPO/BTMAP-Vi cell with 0.5 M electrolyte concentration (A) at frequencies ranging from 1 Hz to 10k Hz. The AC-ASR (high frequency resistance) was 2.24 Ω cm^2. (B) Viscosity of the 0.5 M TMAP-TEMPO aqueous solution at room temperature.
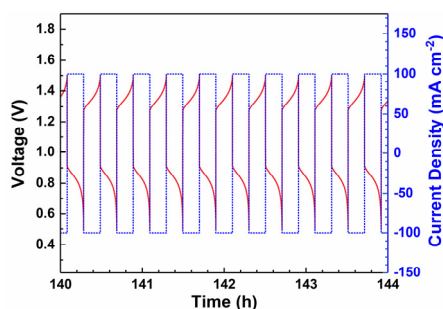
Figure S22. Representative cell voltage and charge/discharge current density vs. time curves during cycling at 100 mA cm^{-2} for TMAP-TEMPO/BTMAP-Vi cell with electrolyte concentration of 0.5 M.
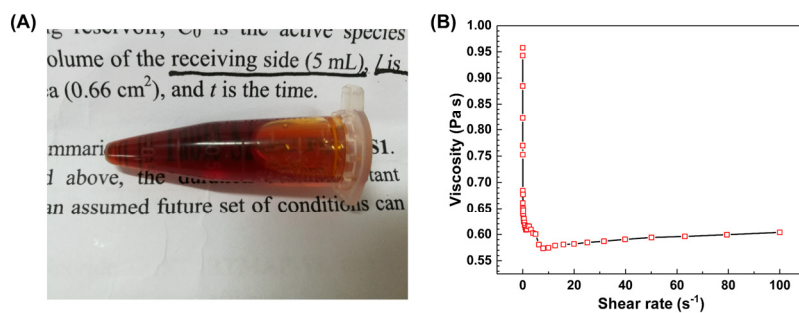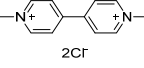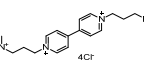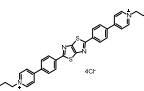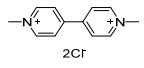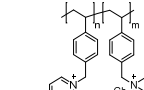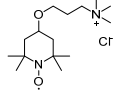
Figure S23 (A) Physical image of a very viscous TMAP-TEMPO solution, by dissolving 1.2 g of TMAP-TEMPO in 200 uL of water. The concentration determined by UV-Vis calibration is 4.5 M. (B) Viscosity of the resulting aqueous TMAP-TEMPO solution, with 4.5 M concentration at room temperature.

Table S1. The diffusion coefficient (D) and electron-transfer rate constant (k_0) of representative redox couples at a glassy carbon electrode.

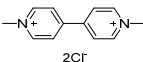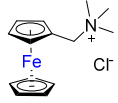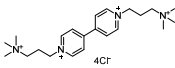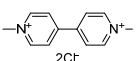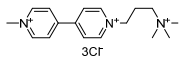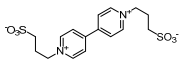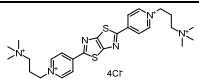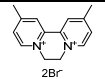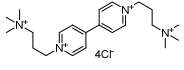| Redox Couple	D (cm^2 s^{-1})	k_0 (cm s^{-1})	References
FcNCl	$3.74×10^{-6}$	$3.66×10^{-5}$ (oxidation)	2
FcN$_2$Br$_2$	$3.64×10^{-6}$	$4.60×10^{-6}$ (oxidation)	2
Alloxazine carboxylate	-	$1.2×10^{-5}$ (reduction)	3
AQDS	$3.81×10^{-6}$	$7.25×10^{-3}$ (reduction)	4
DHAQ	$4.82×10^{-6}$	$7.0×10^{-3}$ (reduction)	5
V^{3+}/V^{2+}	$4×10^{-6}$	$1.7×10^{-5}$ (reduction)	6
VO^{2+}/VO$_2$$^+$	$1.4×10^{-6}$	$7.5×10^{-4}$ (oxidation)	7
4-OH-TEMPO	$2.95×10^{-5}$	$2.6×10^{-4}$ (oxidation)	8
TEMPTMA	$4.8×10^{-6}$	$4.2×10^{-3}$ (oxidation)	9
TEMPO-4-SO$_3$K	$2.98×10^{-6}$	$1.9×10^{-3}$ (oxidation)	10
Poly-TEMPO	$7.0×10^{-8}$	$4.5×10^{-4}$ (oxidation)	11
TMAP-TEMPO	**$3.48×10^{-6}$**	**$1.02×10^{-2}$** (oxidation)	**This work**

Table S2. Comparison of cell performances of relevant flow and hybrid flow batteries utilizing viologen and TEMPO derivatives. Limiting active electrolytes are colored in red and "NA" means data not available.

Negolyte	Posolyte	Redox Potentials (V)		No. of Cycles (No. of hours)	Capacity fade rate (%)		OCV @50% SOC (V)	Reference
		negolyte	posolyte		Per Cycle	Per Hour		
MV	4-OH-TEMPO	-0.45 (vs. NHE)	0.80 (vs. NHE)	100 (~9 h)	>0.11	1.17	1.25	8
BTMAP-Vi	BTMAP-Fc	-0.36 (vs. SHE)	0.39 (vs. SHE)	250 (340 h)	0.0057	0.0042	0.75	12
Zn²⁺/Zn	g⁺-TEMPO	NA	NA	140 (NA)	0.046	NA	1.55	13
[(NPr)₂TTz]Cl₄	Nᴹᵉ-TEMPO	-0.44 (vs. NHE)	1.00 (vs. NHE)	300 (~72 h)	0.03	0.12 (inferred from graph in paper)	1.44	14
Zn²⁺/Zn	TEMPO-4-SO₃K	-1.08 (vs. Ag/AgCl)	0.61 (vs. Ag/AgCl)	50 (55.6 h)	NA (capacity increased)	NA	1.77	10
MV	TEMPTMA	-0.63 (vs. Ag/AgCl)	0.79 (vs. Ag/AgCl)	100 (NA)	0.03 (inferred from graph in paper)	0.046	1.4	9
Viologen polymer	TEMPO polymer	-0.49 (vs. Ag/AgCl)	0.70 (vs. Ag/AgCl)	100 (NA)	0.24	1.12 (inferred from graph in paper)	1.1	11

MV	**FcNCl**	-0.45 (vs. NHE)	0.61 (vs. NHE)	500 (~250)	0.04	0.078	1.05	2
BTMAP-Vi	**TMAP-TEMPO**	-0.38 (vs. SHE)	0.81 (vs. SHE)	1000 (~220 h)	0.007	0.026	1.12	**This work**

Table S3. The comparison of cycling stability of AORFBs using MV-derivatives as the negolyte.

Structure	Concentration of Negolyte	Current Density (mA cm^{-2})	No. of Cycles	Capacity Retention per Cycle	Capacity Retention per Day	Reference
(MV)	0.5 M	60	100	99.88%	96.5%	[8]
	2.0 M	80	100	99.963%	99.72%	[9]
[(Me)(NPr)V]Cl$_3$	0.25 M (2e$^-$)	60	50	99.82%	91.94%	[15]
(SPr)$_2$V	0.5 M	60	300	99.99%	99.55%	[16]
[(NPr)$_2$TTz]Cl$_4$	0.25 M (2e$^-$)	60	50	99.94%	97.31%	[14]
5	0.5 M	5	100	99.8%	99.55%	[17]
BTMAP-Vi	0.5 M	60	500	99.995%	99.78%	[18]
	0.75 M	50	500	99.9989%	99.969%	[12]

The stability of MV-derivatives.

Since the first report of Methyl viologen (MV) based all organic aqueous flow battery by Liu et al. [8], the investigations on MV-derivatives as negative electrolytes (negolytes) for AORFBs have been extensively conducted. The viologens can undergo two separate steps of one electron reduction/oxidation reaction, from MV^{2+} to the cationic free radical MV$^{•+}$ and finally to MV^0. The first step is ideally reversible, while the redox reaction between to neutral MV^0 and MV$^{•+}$ is irreversible and leads to side reactions because of the highly reductive nature and water insolubility of MV^0.

MV cannot be adopted to either basic or acidic solutions because of the attack of ammonium by OH$^-$, resulting in dealkylation and the annihilation of reduced MV by H$^+$ [19]. However, MV and its derivatives have good chemical stability in neutral-pH solutions and early reports on the cycling performance of the viologen-based neutral-pH aqueous flow battery confirmed the stability. We summarized in Table S3 the recent reports of MV derivatives in aqueous organic flow batteries. It is obvious that the stability of MV derivatives has been significantly improved over the years and the stability is closely dependent on the attached substituents.

Till now, two plausible decomposition mechanism has been suggested for MV derivatives. During cell charging, MV^{2+} is reduced to the cation radical, MV$^{•+}$, which can be readily oxidized back to MV^{2+} by O$_2$, forming superoxide anion and eventually leading to the accumulation of OH$^-$. The

accumulated OH^- would attack MV derivatives, causing molecular decomposition. Another mechanism is operative even if oxygen is strictly excluded. The reduced form of viologen, two $MV^{\bullet+}$ undergo fast dimerization to a stable dimer, forming a stable internal charge transfer complex [20]. This dimer can undergo disproportionation to form the MV^{2+} and the doubly reduced MV^0, the latter of which has poor water solubility and could be readily protonated to form another redox-inactive species. [21] [22]

To mitigate such capacity fade, Eugene et al. took advantage of the increased coulombic repulsion of densely charged viologen derivative (BTMAP-Vi), which has less chances of molecular collision. Cell cycling results indicate that the corresponding BTMAP-Vi based aqueous flow battery has a capacity retention rate of 99.9943% per cycle even at a reactant concentration of 1.3 M, projecting a calendar life of around 10 years. The proposed strategy was validated by Tianbiao Liu et al. [18]: BTMAP-Vi is the most stable form among various MV derivatives reported to date.

Supplemental Experimental Procedures

General information

1,3-dichloropropane, 1-bromo-3-chloropropane, 4,4'-bipyridine, methyl tert-butyl ether (MTBE), and anhydrous N, N-dimethylformamide (DMF), were purchased from Energy Chemical Co., Ltd. (Shanghai, China). 4-hydroxy-2,2,6,6-tetramethylpiperidin-1-oxyl (4-OH-TEMPO) was purchased from TCI Chemicals Co., Ltd. (Shanghai, China). Trimethylamine (TMA) tetrahydrofuran solution and acetone were obtained from Sinopharm Chemical Reagent Co., Ltd (Shanghai, China). Isopropanol was purchased from Chengdu Kelong Chemical Reagent Co., Ltd (Chengdu, China). Other chemicals were obtained from domestic vendors and all chemicals were used as received without further purification. Deionized water was used throughout the work. ^{1}H NMR spectra were recorded on AVANCE III HD 400 spectrometers. MS was test on FTMS-cESI.

Synthesis of BTMAP-Vi

To a round-bottom flask were added 1,3-dichloropropane (25.0 g, 221.0 mmol) and TMA tetrahydrofuran solution (53.0 mL, 221.0 mmol). The resulting mixture was stirred at 60 ^{o}C for 96 hours, which was then cooled to room temperature and diluted with ~500 mL of MTBE. The suspended white solid was collected by vacuum filtration, washed several times with MTBE and vacuum dried to give (3-chloro-propyl)-trimethyl-ammonium chloride (16.0 g, yield: 42.1%).

7.2 g (41.8 mmol) of (3-chloro-propyl)-trimethyl-ammonium chloride and 3.26g (20.9 mmol) of 4,4'-bipyridine were suspended in anhydrous DMF (~20 mL) and the resultant mixture was heated to reflux under Ar. Upon heating, all solids dissolved. After heating for 1 hour, the reaction mixture was cooled to room temperature and the mixture solidified upon cooling. Then, isopropanol (~200 mL) was added and the solid material was triturated. The precipitate was filtered off, washed with isopropanol, then acetone, and finally dried in vacuo to give (3-trimethylammonio) propyl viologen tetrachloride (BTMAP-Vi). Yield: 3.11 g (29.9%) of a pale-white solid. ^{1}H NMR (400MHZ, D$_2$O): δ 9.24 (d, 4H), 8.66 (d, 4H), 4.90 (t, 4H), 3.63 (m, 4H), 3.24 (s, 18H), 2.73 (m, 4H).

Synthesis of TMAP-TEMPO

To a mixture of toluene (4.5 mL) and 50% aqueous sodium hydroxide (15 mL), 4-OH-TEMPO (4.5 g, 25.5 mmol), tetrabutylammonium bromide (TBAB, 0.39 g, 1.2 mmol) and 1-bromo-3-chloropropane (16.1 g, 102.0 mmol) were added and the resulting mixture was vigorously stirred at room temperature for 48 h. Upon completion, ~150 mL of ether was added, and the obtained mixture was washed with water (100 mL × 10). The organic layer was collected, dried over anhydrous sodium sulfate and then evaporated, giving a viscous red liquid. The residue was finally purified by flash column chromatography on silica gel (EtOAc: hexane = 1:20) to afford the desired product 4-(2,2,6,6-tetramethyl-1-oxyl-4-piperidoxyl) propyl chloride (Pr-TEMPO, 2.62 g, 33.4%) as a viscous red liquid. The synthesized Pr-TEMPO was reduced by phenyl hydrazine for ^{1}H NMR test. ^{1}H NMR (400MHZ, DMSO-d$_6$): δ 3.69 (t, 2H), 3.58 (m, 1H), 3.53 (t, 2H), 1.95 (m, 4H), 1.31 (m, 2H), 1.12 (d, 12H). HRMS(ESI) 248.1414, calc. for C$_{12}$H$_{23}$O$_2$NCl, 248.1417.

To a round-bottom flask were added Pr-TEMPO (2.62 g, 10.5 mmol) and 25.0 mL of TMA alcohol solution (4.2 mol L^{-1}, 105.0 mmol). After stirring at room temperature for 48 h, the reaction mixture was concentrated under reduced pressure. The obtained viscous liquid was dissolved in DI water (~50 mL) and repeatedly washed with ether (100 mL×10). Drying the aqueous layer under reduced

pressure gave a red viscous liquid of 4-(2,2,6,6-tetramethyl-1-oxyl-4-piperidoxyl) propyl-trimethyl-ammonium chloride (TMAP-TEMPO, 2.05 g, 63.3%), which solidified during storage. The synthesized TMAP-TEMPO was reduced by phenyl hydrazine for ^{1}H NMR test. ^{1}H NMR (400MHZ, DMSO-d$_6$): δ 3.60 (m, 1H), 3.47 (t, 2H), 3.36 (t, 2H), 3.09 (s, 9H), 1.93 (m, 4H), 1.32 (t, 2H), 1.14 (d, 12H). HRMS(ESI) m / z: exp. 272.2459, calc. for $C_{12}H_{32}O_2N_2$, 272.2458.

Solubility and viscosity tests.

The solubility of TMAP-TEMPO in water was estimated by adding ~1.2 g TMAP-TEMPO to 200 μL of water, (yielding a homogeneous solution of around 800 μL). All the solid materials dissolved immediately and resulted in a very viscous red solution (Figure S20A), the viscosity of which was determined by ZNN-D12 (Figure S20B). This viscous red solution was then diluted by a known factor and concentration of the diluted solution was calibrated by UV-Vis (Persee, TU-1901, spectrophotometer), according to a pre-established absorbance-concentration curve. Although we are sure that more solid could be further dissolved, we did not further test the solubility limit because simply of the high viscosity of the solution.

We test the accurate solubility of TMAP-TEMPO by determining the concentration of Cl$^-$ via ion chromatography (IC). Specifically, an aqueous solution of TMAP-TEMPO was prepared by adding 0.65g of TMAP-TEMPO into 100 μL of water, from which 20 μL of saturated solution was extracted and then diluted to 100 mL. Chloride ion concentration of the samples were determined by IC and the solubility of TMAP-TEMPO was calculated as follows. This was repeated for four times and an average was made.

(1) The average Cl$^-$ concentration (C_{Cl^-}) of the samples is:

$$C_{Cl^-} = \frac{36.40+30.46+32.24+31.79}{4} \times \frac{100 \text{ mL}}{20\times10^{-3}\text{mL}} \text{ μg mL}^{-1}$$

$$=1.64\times10^5 \text{ μg mL}^{-1} = \frac{1.64\times10^5\times10^{-6}\times10^3}{35.45} \text{ mol L}^{-1}=4.62 \text{ mol L}^{-1}$$

(2) The concentration of TMAP-TEMPO ($C_{TMAP\text{-}TEMPO}$) equals to C_{Cl^-}.

$$C_{TMAP\text{-}TEMPO}=C_{Cl^-}=4.62 \text{ mol L}^{-1}$$

   Therefore, the accurate solubility of TMAP-TEMPO in water was 4.62 M at room temperature.

Permeability measurements.

The permeability of 4-OH-TEMPO, TMAP-TEMPO or BTMAP-Vi across the Selemion® AMV anion-selective membrane was evaluated with a lab-made two-compartment cell [23]. The donating side was filled with an 0.1 M of electrolyte in 1 M NaCl aqueous solution and the receiving side was filled with 1 M NaCl aqueous solution. Both the donating and the receiving compartments were filled with the same volume of solutions and continuously agitated with stirring rods. At different time intervals, aliquots were taken from the receiving side, diluted and characterized by UV-Vis spectrophotometry and the concentration was calculated from a calibration curve. The permeability was then calculated based on the slope of a linear regression of concentration in the receiving compartment vs. time, using Fick's law as embodied in the following equation:

$$P=\frac{c_t V_0 l}{At(c_0-c_t)} \approx \frac{c_t V_0 l}{Atc_0}.$$

Herein, P is the permeability (cm^2 s^{-1}), A is the effective membrane area (1.86 cm^2), t is the elapsed

time (s), c_t is the concentration of active species in the receiving side at time t (mol L^{-1}), V_0 is the volume of the solution in either compartment (15 mL), l is the thickness of the membrane (125 μm), and c_0 is the concentration of electrolyte in the donating compartment (0.1 mol L^{-1}), and c_t is kept at least two orders of magnitude lower than c_0.

Electrochemical Studies.

Cyclic voltammetry (CV) studies were carried out in 1.0 M NaCl aqueous solution, as the supporting electrolyte, with a ZENNIUM E electrochemical workstation (ZAHNER, Germany). Glassy carbon (3 mm diameter), Ag/AgCl (0.2046 V vs SHE), and platinum coil were used as working electrode, reference electrode and counter electrode, respectively. The glassy carbon electrode was polished with alumina slurry (0.5 μm) and rinsed with deionized H$_2$O prior to measurement.

Rotating-disk-electrode (RDE) studies. RDE measurements were carried out using a CHI600E potentiostat (CH Instruments, Inc., Austin, US) and a Pine E4TQ RDE. A 5-mm diameter glassy carbon rotating electrode was used as the working electrode, which was thoroughly polished prior to use. The Ag/AgCl reference electrode and platinum coil counter electrode were used. Linear sweep voltammetry (LSV) scans were recorded at a scan rate of 5 mV s^{-1} from 0.2 V to 1.2 V versus SHE, with rotational speed between 100-3600 ppm. At each rotation rate three scans were recorded and averaged to ensure reproducible results. Background scans were also taken with blank supporting electrolyte solution and subtracted. A Levich plot of the limited current vs. the square root of the rotation speed was constructed. The diffusion coefficient of TMAP-TEMPO was calculated from the slope of the linear fitting according to Levich equation: $i=0.620\, nFAcD^{2/3}v^{-1/6}\omega^{1/2}$, where n = 1, Faraday's constant F = 96485 C mol^{-1}, electrode area A = 0.196 cm^2, molar concentration c = 1 mol cm^{-3}, the kinematic viscosity u = 9.56×10^{-3} cm^2 s^{-1} (1 M NaCl aqueous solution), and D represents the diffusion coefficient. The diffusion coefficient for the oxidation of TMAP-TEMPO was calculated to be 3.48 ×10^{-6} cm^2 s^{-1}. The Tafel equation relating the kinetic current (i_K) for the oxidation of TMAP-TEMPO and the overpotential (η), $\log_{10}(i_k)=\log_{10}(nFcAk_0)+\alpha nF\eta/2.303RT$, was used to deduce the rate constant and transfer coefficient (α). The rate constant and the transfer coefficient for the oxidation of TMAP-TEMPO were calculated to be 1.02 ×10^{-2} cm s^{-1} and 0.576, respectively.

Full cell tests. Cell hardware was purchased from Fuel Cell Tech (Albuquerque, US) and pyrosealed POCO graphite flow plates with serpentine flow fields were used on both sides. The electrode on each side comprised 3 stacked sheets of Sigracet SGL 39AA carbon paper electrodes (baked at 400 °C for 24 h prior to use) of 5 cm^2 geometric area. A sheet of anion-exchange membrane (AMV, 125 μm thickness, Selemion®, Japan) was sandwiched between the positive and the negative electrodes with the effective area of 5 cm^2. The space between the flow plates was well-sealed with Viton gaskets. The electrolytes were pumped through the cell stack at a flow rate of 60 rpm using *Masterflex L/S* peristaltic pump (Cole-Parmer, Vernon Hills, IL). For the 0.1 M cell, the posolyte comprises either 10 mL of 0.1 M TMAP-TEMPO in 1 M NaCl aqueous solution or 10 mL of 0.1 M 4-OH-TEMPO in 1 M NaCl aqueous solution, and the negolyte comprises 15 mL of 0.1 M BTMAP-Vi in 1 M NaCl aqueous solution. For the 0.5 M cell, the posolyte comprises 10 mL of 0.5 M TMAP-TEMPO in 1 M NaCl aqueous solution, and the negolyte comprises 15 mL of 0.5 M

BTMAP-Vi in 1 M NaCl aqueous solution. For the 1.5 M cell, the posolyte comprises 5 mL of 1.5 M TMAP-TEMPO in 4.5 M NaCl aqueous solution, and the negolyte comprises 7.5 mL of 1.5 M BTMAP-Vi aqueous solution. Polarization curves were acquired by charging the cell to certain states of charge (SOC), then polarized by linear sweep voltammetry on a Bio-Logic BCS-815. Galvanostatic cell cycling was performed at the varied current densities of 10, 20, 40, 60, 80 and 100 mA cm^{-2} with cutoff voltages at 1.5 V for the charge process and 0.5 V for the discharge process. Potentio-controlled electrochemical impedance spectroscopy (EIS) was recorded as needed at frequencies ranging from 1 Hz to 10kHz.

Unbalanced compositionally-symmetric cell cycling method. 5 mL of 50% SOC 0.1 M TMAP-TEMPO in 1M NaCl was placed in one reservoir of a flow cell as a capacity limiting side (CLS), and 10 ml of the same 50% SOC electrolyte was placed in the other reservoir as a non-capacity limiting side (NCLS). With a 0.0 V open circuit potential, the cell was cycled potentiostatically (to avoid transient ohmic effects) between ±200 mV with a current cutoff of 1 mA cm^{-2}.

Calculation of capacity loss due to electrolyte crossover. The capacity loss of each cycle due to electrolyte crossover is calculated according to the following equation:

$$Q_{perm}=Fn_{perm}\approx F\frac{PAtc_0}{l}$$

Where, Q_{perm} represents the capacity loss due to electrolyte crossover across the membrane, n_{perm} is the molar amount of the corresponding electrolyte, F is the Faraday's constant (96485 C mol^{-1}), P is the permeability of the active electrolyte across the membrane, A is the effective membrane area (5 cm^2), t is the time every cycle took, c_0 is the concentration of donating side (0.1 M), and l is the thickness of the membrane (125 μm).

For a 0.1 M TMAP-TEMPO/BTMAP-Vi or 4-OH-TEMPO/BTMAP-Vi cell assembled herein, the negolyte is 1.5 times electron excess and the capacity loss, Q_{perm}, is dominated by the crossover of the posolyte molecules.

1) For 0.1 M TMAP-TEMPO/BTMAP-Vi cell ($P_{TMAP-TEMPO}$=6.40×10^{-10} cm^2 s^{-1} and t=755 s, time is for every cycle).

$$Q_{perm}^{TMAP-TEMPO}=Fn_{perm}=F\frac{P_{TMAP-TEMPO}Atc_0}{l}=96485\times\frac{6.40\times10^{-10}\times5\times755\times0.1\times10^{-3}}{125\times10^{-4}}C=1.86\times10^{-3}C$$

The ratio of crossover capacity loss, $Q_{perm}^{TMAP-TEMPO}$ to the total capacity loss per cycle (Q_{total}) is calculated as follows.

$$\frac{Q_{perm}^{TMAP-TEMPO}}{Q_{total}}\times100\%=\frac{1.86\times10^{-3}C}{4.69\times10^{-3}C}\times100\%=39.6\%$$

2) For 0.1 M 4-OH-TEMPO/BTMAP-Vi cell ($P_{4-OH-TEMPO}$=1.34×10^{-9} cm^2 s^{-1} and t=685 s, time is for every cycle).

$$Q_{perm}^{4-OH-TEMPO}=Fn_{perm}=F\frac{P_{4-OH-TEMPO}Atc_0}{l}=96485\times\frac{1.34\times10^{-9}\times5\times685\times0.1\times10^{-3}}{125\times10^{-4}}C=3.54\times10^{-3}C$$

The ratio of crossover capacity loss, $Q_{perm}^{4-OH-TEMPO}$ to the total capacity loss per cycle (Q_{total}) is calculated as follows.

$$\frac{Q_{perm}^{4\text{-}OH\text{-}TEMPO}}{Q_{total}} \times 100\% = \frac{3.54 \times 10^{-3}C}{3.75 \times 10^{-2}C} \times 100\% = 9.44\%$$

3) The ratio of capacity saved every cycle because of the lower permeability of TMAP-TEMPO than that of 4-OH-TEMPO to the total capacity savings is:

$$\gamma = \frac{3.54\text{-}1.86}{37.5\text{-}4.69} \times 100\% = 5.12\%$$

Supplemental References

1. Goulet, M.-A., Aziz M.J. (2018). Flow battery molecular reactant stability determined by symmetric cell cycling methods. J. Electrochem. Soc. 165, A1466-A1477.

2. Hu, B., DeBruler C., Rhodes Z., Liu T.L. (2017). Long-Cycling Aqueous Organic Redox Flow Battery (AORFB) toward Sustainable and Safe Energy Storage. J. Am. Chem. Soc. 139, 1207-1214.

3. Lin, K., Gomez-Bombarelli R., Beh E.S., Tong L., Chen Q., Valle A., Aspuru-Guzik A., Aziz M.J., Gordon R.G. (2016). A redox-flow battery with an alloxazine-based organic electrolyte. Nat. Energy 1, 16102.

4. Huskinson, B., Marshak M.P., Suh C., Er S., Gerhardt M.R., Galvin C.J., Chen X., Aspuru-Guzik A., Gordon R.G., Aziz M.J. (2014). A metal-free organic-inorganic aqueous flow battery. Nature 505, 195-198.

5. Lin, K., Chen Q., Gerhardt M.R., Tong L., Kim S.B., Eisenach L., Valle A.W., Hardee D., Gordon R.G., Aziz M.J., et al. (2015). Alkaline quinone flow battery. Science 349, 1529-1532.

6. Sum, E., Skyllas-Kazacos M. (1985). A study of the V(II)/V(III) redox couple for redox flow cell applications. J. Power Sources 15, 179-190.

7. Sum, E., Rychcik M., Skyllas-kazacos M. (1985). Investigation of the V(V)/V(IV) system for use in the positive half-cell of a redox battery. J. Power Sources 16, 85-95.

8. Liu, T., Wei X., Nie Z., Sprenkle V., Wang W. (2016). A Total Organic Aqueous Redox Flow Battery Employing a Low Cost and Sustainable Methyl Viologen Anolyte and 4-HO-TEMPO Catholyte. Adv. Energy Mater. 6, 1501449.

9. Janoschka, T., Martin N., Hager M.D., Schubert U.S. (2016). An Aqueous Redox-Flow Battery with High Capacity and Power: The TEMPTMA/MV System. Angew. Chem. Int. Ed. 55, 14425-14428.

10. Winsberg, J., Stolze C., Schwenke A., Muench S., Hager M.D., Schubert U.S. (2017). Aqueous 2,2,6,6-Tetramethylpiperidine-N-oxyl Catholytes for a High-Capacity and High Current Density Oxygen-Insensitive Hybrid-Flow Battery. ACS Energy Lett. 2, 411-416.

11. Janoschka, T., Martin N., Martin U., Friebe C., Morgenstern S., Hiller H., Hager M.D., Schubert U.S. (2015). An aqueous, polymer-based redox-flow battery using non-corrosive, safe, and low-cost materials. Nature 527, 78-81.

12. Beh, E.S., De Porcellinis D., Gracia R.L., Xia K.T., Gordon R.G., Aziz M.J. (2017). A neutral pH aqueous organic-organometallic redox flow battery with extremely high capacity retention. ACS Energy Lett. 2, 639-644.

13. Chang, Z., Henkensmeier D., Chen R. (2017). One-Step Cationic Grafting of 4-Hydroxy-TEMPO and its Application in a Hybrid Redox Flow Battery with a Crosslinked PBI Membrane. ChemSusChem 10, 3193-3197.

14. Luo, J., Hu B., Debruler C., Liu T.L. (2018). A pi-Conjugation Extended Viologen as a Two-Electron Storage Anolyte for Total Organic Aqueous Redox Flow Batteries. Angew. Chem. Int. Ed. 57, 231-235.

15. DeBruler, C., Hu B., Moss J., Liu X., Luo J., Sun Y., Liu T.L. (2017). Designer two-electron storage viologen anolyte materials for neutral aqueous organic redox flow batteries. Chem 3,

961-978.

16. DeBruler, C., Hu B., Moss J., Luo J., Liu T.L. (2018). A Sulfonate-Functionalized Viologen Enabling Neutral Cation Exchange, Aqueous Organic Redox Flow Batteries toward Renewable Energy Storage. ACS Energy Lett. 3, 663-668.

17. Huang, J., Yang Z., Murugesan V., Walter E., Hollas A., Pan B., Assary R.S., Shkrob I.A., Wei X., Zhang Z. (2018). Spatially Constrained Organic Diquat Anolyte for Stable Aqueous Flow Batteries. ACS Energy Lett. 3, 2533-2538.

18. Hu, B., Tang Y., Luo J., Grove G., Guo Y., Liu T.L. (2018). Improved radical stability of viologen anolytes in aqueous organic redox flow batteries. Chem. Commun. 54, 6871-6874.

19. Bird, C., Kuhn A. (1981). Electrochemistry of the viologens. Chem. Soc. Rev. 10, 49-82.

20. Murugavel, K. (2014). Benzylic viologen dendrimers: a review of their synthesis, properties and applications. Polym. Chem. 5, 5873-5884.

21. Bard, A., Ledwith A., Shine H. (1976). Formation, properties and reactions of cation radicals in solution. Adv. Phys. Org. Chem. 13, 155-278.

22. Venturi, M., Mulazzani Q.G., Hoffman M.Z. (1984). Radiolytically-induced one-electron reduction of methyl viologen in aqueous solution: Stability of the radical cation in acidic and highly alkaline media (1). Radiat. Phys. Chem. (1977) 23, 229-236.

23. Yang, Z., Tong L., Tabor D.P., Beh E.S., Goulet M.A., Porcellinis D., Aspuru‐Guzik A., Gordon R.G., Aziz M.J. (2017). Alkaline Benzoquinone Aqueous Flow Battery for Large‐Scale Storage of Electrical Energy. Adv. Energy Mater. 8, 1702056.